

pubs.acs.org/est Article

Using Infrared Photothermal Heterodyne Imaging to Characterize Micro- and Nanoplastics in Complex Environmental Matrices

Kirill Kniazev, Ilia M. Pavlovetc, Shuang Zhang, Junyeol Kim, Robert L. Stevenson, Kyle Doudrick,* and Masaru Kuno*



Cite This: https://doi.org/10.1021/acs.est.1c05181



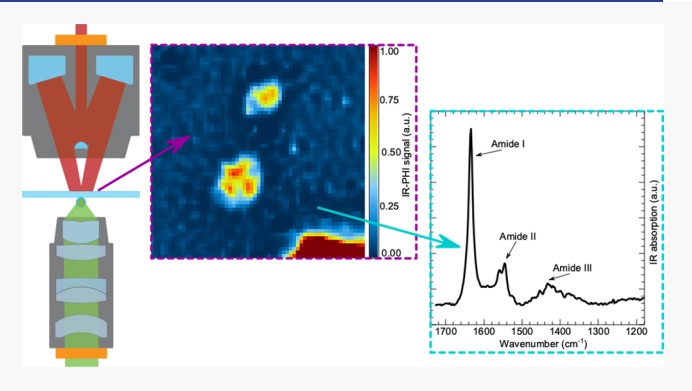
ACCESS

III Metrics & More

Article Recommendations

Supporting Information

ABSTRACT: A key challenge for addressing micro- and nanoplastics (MNPs) in the environment is being able to characterize their chemical properties, morphologies, and quantities in complex matrices. Current techniques, such as Fourier transform infrared spectroscopy, provide these broad characterizations but are unsuitable for studying MNPs in spectrally congested or complex chemical environments. Here, we introduce a new, superresolution infrared absorption technique to characterize MNPs, called infrared photothermal heterodyne imaging (IR-PHI). IR-PHI has a spatial resolution of $\sim\!\!300$ nm and can determine the chemical identity, morphology, and quantity of MNPs in a single analysis with high sensitivity. Specimens are supported on CaF2 coverslips under ambient conditions from where we (1) quantify



MNPs from nylon tea bags after steeping in ultrapure water at 25 and 95 °C, (2) identify MNP chemical or morphological changes after steeping at 95 °C, and (3) chemically identify MNPs in sieved road dust. In all cases, no special sample preparation was required. MNPs released from nylon tea bags at 25 °C were fiber-like and had characteristic IR frequencies corresponding to thermally extruded nylon. At 95 °C, degradation of the nylon chemical structure was observed via the disappearance of amide group IR frequencies, indicating chain scission of the nylon backbone. This degradation was also observed through morphological changes, where MNPs altered shape from fiber-like to quasi-spherical. In road dust, IR-PHI analysis reveals the presence of numerous aggregate and single-particle ($<3 \mu m$) MNPs composed of rubber and nylon.

KEYWORDS: microplastics, nanoplastics, plastics, elastomer, polymer, environment, IR-PHI, infrared, spectroscopy, microscopy, mid-infrared, FTIR, photothermal, super-resolution, infrared photothermal heterodyne imaging

■ INTRODUCTION

Micro- and nanoplastics (MNPs) are an emerging contaminant classification formed from the direct release or breakdown of polymer-based products. They are ubiquitous in the environment, stretching from urban environments¹ to remote Arctic locations.² As a result, they have been detected in foods and humans,³⁻⁶ and their ecological toxicity is now becoming apparent.⁷⁻⁹ The physical—chemical properties (e.g., polymer type, size) of MNPs are driving forces behind their toxicity and environmental behavior. The environmental history of MNPs also plays a role in their fate and toxicity, as degraded MNPs (e.g., from heat¹⁰ or sunlight^{11,12}) possess different chemical properties from their starting parent polymers. Properly addressing the environmental and human health risks of MNPs require robust characterization and quantification analytics, but there is currently a lack of reliable methods.

Numerous analytical approaches exist to characterize and quantify MNPs. 13-15 Optical and electron microscopy are commonly used techniques, 16,17 but they do not provide detailed information about the chemical composition of

samples, and they are laborious. Mass spectrometric approaches such as pyrolysis gas chromatography—mass spectrometry and thermal desorption gas chromatography—mass spectrometry search can characterize the polymer type and its chemical additives. These techniques, however, are destructive and yield no information about MNP size or morphology. Vibrational spectroscopy/microscopy approaches [for example, Fourier transform infrared (FTIR) and Raman] have also been used to characterize NMPs. They are non-destructive, can identify polymer type, and can quantify MNP concentrations. Unfortunately, these traditional vibrational spectroscopic/microscopic approaches possess spatial resolutions dictated by the optical diffraction limit. 19—25 This hinders their

Received: August 2, 2021 Revised: October 20, 2021 Accepted: October 21, 2021



application to complex, spectrally crowded environmental samples. For FTIR, a lower limit spatial resolution is approximately 5 μ m. Raman microscopy uses visible light to realize a significantly better spatial resolution, limited by the diffraction limit of visible light. Its utility is hindered by low specimen Raman scattering cross-sections approximately 10 orders of magnitude smaller than corresponding infrared absorption cross sections. Therefore, specialized plasmonic substrates are often needed to increase Raman intensities in analytical sensing applications. ²⁶

Herein, we demonstrate the use of a new technique to characterize MNPs in environmental samples called infrared photothermal heterodyne imaging (IR-PHI). 27,28 IR-PHI is a super-resolution infrared absorption technique that possesses the spatial resolution of Raman microscopy/spectroscopy while simultaneously taking advantage of large infrared absorption cross sections to achieve superior sensitivity. In brief, IR-PHI detects infrared absorption based on temperature-induced changes to specimen refractive indices and scattering cross sections. Infrared radiation, on resonance with a specimen's vibrational transitions, converts into a local temperature difference (ΔT) of order 1 K.²⁸ Measurable changes to scattering cross sections result, especially when the intensity of the incident infrared light is modulated to make refractive index changes (Δn) periodic. These periodic in-time Δn variations can, in turn, be detected via intensity modulation induced upon a second, continuous wave probe laser. More details about IR-PHI, its development, and its implementation can be found in recent reviews. 27,29

IR-PHI can identify MNP type, size and morphology, and quantity. IR-PHI's spatial resolution is dictated by its probe wavelength. This blends the high resolution and sensitivity of visible wavelength microscopy with the chemical specificity of IR spectroscopy. A ~300 nm spatial resolution has been demonstrated using a visible probe laser. 30,31 Although this spatial resolution is similar to Raman, IR-PHI possesses superior sensitivity due to an intrinsically larger infrared absorption cross section compared to Raman scattering cross sections, and IR-PHI has a lower theoretical limit that can be reached using advanced algorithms. Demonstrations of concerted IR-PHI sensitivity and high spatial resolution have involved measuring the infrared absorption of individual polymer nanoparticles, 28,30 individual metal nanostructures, 32 semiconductors, ^{33,34} individual lipid droplets, ³⁵ single viruses, ³⁶ proteins, ³⁷ and cells. ^{30,38} IR-PHI's combination of high spatial resolution and sensitivity thus makes it a viable technique for interrogating MNPs in spectroscopically congested, environmental samples.

Herein, we demonstrate the first use of IR-PHI to characterize the chemical identity, size and morphology, and quantity of MNPs released from consumer products into the environment. The method was first validated using polymethylmethacrylate (PMMA) microspheres of a known size and quantity. We then used the method to characterize MNPs released from nylon tea bags that had been steeped in water at 25 and 95 °C. Finally, IR-PHI was used to characterize the chemical identity of single MNPs detected in road dust, an environmentally complex sample containing polymers particles from tread wear of tire thermoplastics. 39–42

MATERIALS AND METHODS

Sample Collection and Preparation. PMMA Microspheres. PMMA microspheres in water and <0.1% NaN₃ as a

preservative were obtained from Magsphere, Inc. (Lot no. PM4652A-0319). The manufacturer reported diameter was 750 nm \pm 10% (radius 375 nm \pm 10%) and the solution concentration was 10% w/v. The solution was diluted with ultrapure water (18.2 $M\Omega \times cm)$ before use.

Nylon MNPs. Nylon MNPs were obtained from tea bags. Nylon tea bags were purchased locally and cut with scissors to empty their contents. Emptied tea bags were rinsed with ultrapure water thrice to remove any remaining tea leaf debris. Samples were dried in a covered glass beaker in a fume hood to minimize any potential environmental contamination. To make MNP solutions, 1 tea bag was added to 150 mL of ultrapure water and heated at ~95 °C for 5 min. The tea bag was then removed and the remaining MNP aqueous suspension was stored in a glass vial. The resulting particle mass, as weighed by a microbalance, was approximately 1.35 mg. A sample was produced in a similar manner at ~25 °C (room temperature water), and a control sample was made by collecting boiled ultrapure water (no MNPs found, data not shown).

Road Dust. Road dust samples were collected from a street sweeper that operates in the region around the University of Notre Dame. ⁴³ Samples were passed through an ASTM E11 no. 200 sieve using a shaker for 1 h to obtain particles with a size <75 μ m. No other preparation steps were required, such as the removal of organic matter. Aqueous suspensions of sieved particles were prepared at 10.29 mg/L (18 mg in 1.75 mL) in ultrapure water for further analyses.

IR-PHI Measurements. The IR-PHI method for analyzing MNPs was first developed and validated using PMMA microspheres of a known size. Chemical identity and size were analyzed for single particles ($N \sim 200$) and the concentration of the prepared aqueous samples was validated using a blind study. Blind samples were prepared by Lab A and then passed to Lab B for IR-PHI analysis. After validating the efficacy using PMMA, the IR-PHI method was used to analyze MNPs released from nylon tea bags during steeping as well as in road dust. For nylon tea bags, IR-PHI was used to characterize changes to the chemical identity, morphology and size, and concentration. For road dust, IR-PHI was used to characterize the chemical identity of single particles.

IR-PHI specimens were made by drop casting bathsonicated MNP suspensions onto CaF₂ coverslips (25.0 mm × 0.5 mm thickness, Crystran) followed by drying under ambient conditions. MNP samples were vigorously shaken before drop casting. All CaF2 coverslips were pre-cleaned with methanol and acetone, followed by subsequent flaming with a propane torch. The droplet volume (0.25 to 2 mL) was chosen based on the MNP concentration with a target coverslip coverage of approximately 1 particle μm^{-2} . This allowed particles to remain discrete while being concentrated enough that they were easily analyzed. To obtain optimal imaging and counting results, samples with unknown MNP concentrations were prepared through a trial-and-error approach. Samples were first prepared at high concentrations and were then diluted down until individual particles were visualized in IR-PHI. Though not done herein, for dilute aqueous samples (e.g., lake), a pre-concentration step (e.g., rotary evaporation or freeze drying) would be required followed by trial-and-error dilution until optimal conditions were achieved. Specific instrument details of IR-PHI can be found in the Supporting Information.

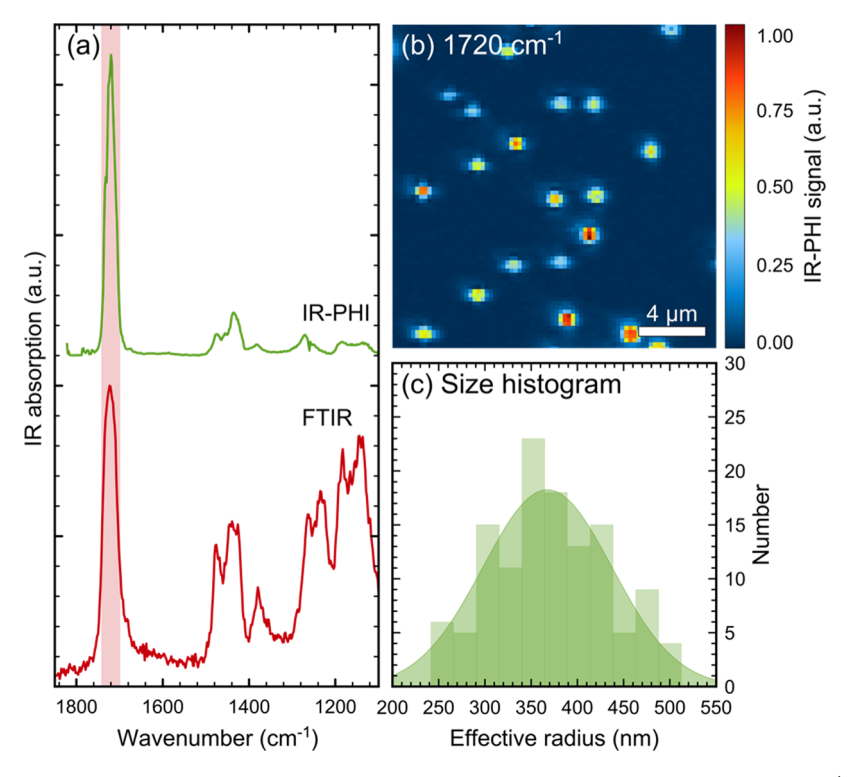


Figure 1. (a) Single-particle IR-PHI and bulk FTIR spectra of PMMA microspheres. Spectra are offset for clarity. (b) $20 \times 20 \ \mu m^2$ false-color image of the IR-PHI raster scan at 1720 cm⁻¹ [highlighted red area in panel (a)]. (c) Size distribution histogram of ~200 PMMA microspheres.

Chemical identity (i.e., IR spectra) was established directly from particle IR-PHI analysis, and images were generated by raster scanning areas of the sample at a target IR frequency. Images were deconvoluted and then processed in ImageJ for subsequent particle counting and sizing . IR-PHI images were collected using a closed-loop piezo stage, under mutual pump and probe foci. Pump wavelengths were tuned to be on resonance with characteristic MNP vibrational transitions. Imaged areas are limited by the nanopositioner scanning range $(300 \times 300 \ \mu\text{m}^2)$. Typical scan areas are $20 \times 20 \ \mu\text{m}^2$ with an image acquisition time of 20 min for the following parameters (piezo step size: 100 nm; lock-in integration time: 30 ms). Individual MNP infrared absorption spectra were acquired by positioning individual particles under pump and probe foci and scanning incident pump wavelengths across either OPO's tuning range.

Given that IR-PHI images are convoluted with the instrument's point spread function (PSF), image deconvolution is performed on all acquired data. Deconvolution is performed using the Richardson–Lucy deconvolution algorithm in scikit-image, an open-source image processing library for the Python programming language. Details of the deconvolution process can be found in the Supporting Information, including before/after IR-PHI images (Figures S1, S2), an image of the instrument PSF (Figure S3), and an overview of the Richardson–Lucy algorithm.

Particle sizes and counts were analyzed using ImageJ. Detailed information can be found in the Supporting Information. IR-PHI's limit of detection (LOD) and spatial resolution have previously been estimated. 27,28,30 For measurements conducted on individual 50 to 550 nm radius (r) polystyrene (PS) or PMMA microspheres, a raw (i.e., without deconvolution) spatial resolution of \sim 350 nm was observed when using a probe wavelength of 532 nm. 28 A spatial

resolution of ~300 nm was subsequently observed by applying the Richardson–Lucy deconvolution algorithm. In terms of sensitivity, an estimated number of detected styrene monomers $(M_{\rm w}=104~{\rm g~mol^{-1}})$ within an individual r=50 nm PS bead is approximately 3×10^7 . This corresponds to an IR-PHI 1450 cm⁻¹ cross section of $\sigma=4.2\times10^{-13}~{\rm cm^2}$. When extrapolated to smaller sizes, a signal-to-noise dictated cross-section LOD is $\sigma_{\rm LOD}=3\times10^{-14}~{\rm cm^2}$ and corresponds to a r=30 nm PS bead. Assuming a similar infrared absorption cross section for nylon's amide I C=O stretch (1637 cm⁻¹), this implies that IR-PHI is able to detect a single $r\sim30$ nm nylon bead (signal to noise ratio of 5, total absorption cross section of $\sigma\sim3\times10^{-14}~{\rm cm^2}$, and apparent $r\sim300$ nm size due to the instrument's finite PSF).

Other Characterization. Bulk FTIR measurements were conducted using a Bruker Tensor 27 FTIR equipped with a ZnSe attenuated total reflectance (ATR) crystal. Scanning electron microscopy (SEM) images of MNPs were acquired using an FEI Magellan 400 SEM operating at an accelerating voltage of 1 kV. SEM specimens were prepared on CaF_2 coverslips with approximately ~ 2 nm of Ir sputtered onto samples to minimize charging during measurements.

■ RESULTS AND DISCUSSION

Analysis of PMMA Microspheres. PMMA microspheres were used to validate IR-PHI for characterizing the chemical identity, size and morphology, and quantity of MNPs. Single-particle IR-PHI and bulk FTIR analyses of the PMMA showed the presence of a predominant absorption band at approximately 1720 cm⁻¹ (Figure 1a), attributed to the C=O stretching of PMMA's ester group. To validate the ability of IR-PHI to size and count MNPs, two blind samples were prepared by lab A (known theoretical concentration and size) and then analyzed with IR-PHI by lab B (unknown). Figure 1b

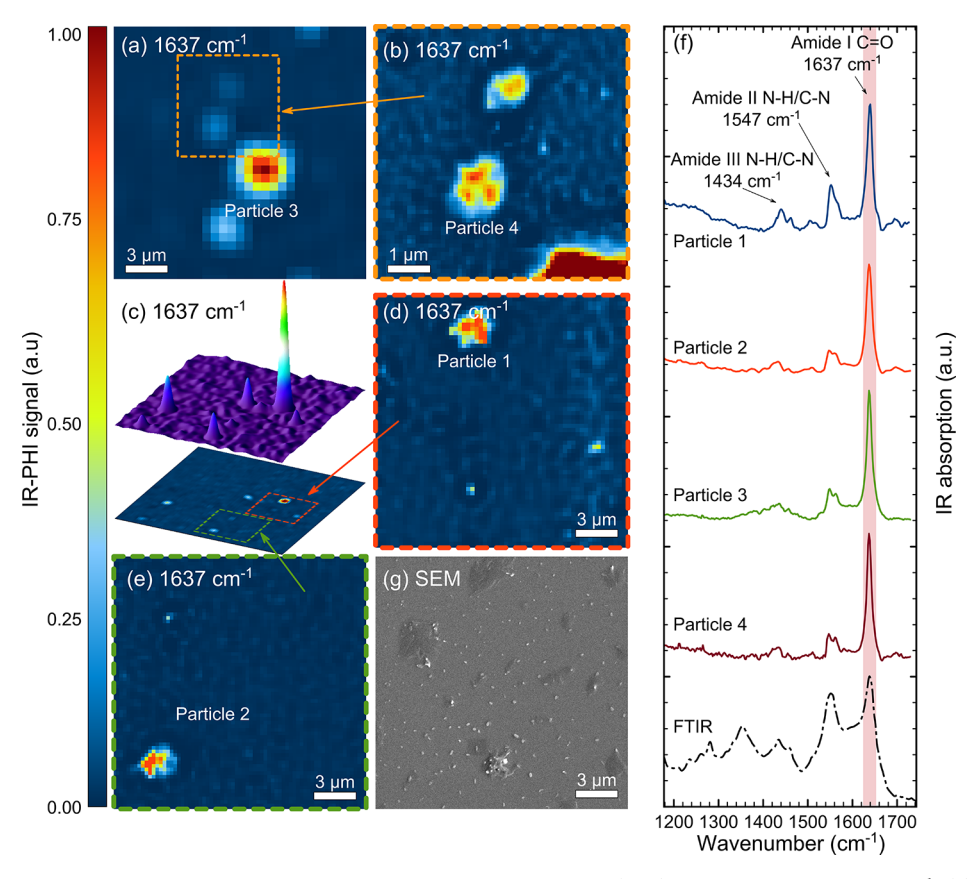


Figure 2. Analysis of MNPs from nylon tea bags steeped at 95 °C. All IR-PHI images (a–e) were analyzed at 1637 cm⁻¹. (a) $15 \times 15 \ \mu m^2$ image depicting four particles. (b) Magnified $6 \times 6 \ \mu m^2$ image of the area highlighted in orange in (a). (c) Low magnification, $50 \times 50 \ \mu m^2$, image and corresponding 3-D surface plot. (d,e) $15 \times 15 \ \mu m^2$ scan of the marked areas in (c). (g) High magnification $15 \times 15 \ \mu m^2$ SEM image of MNPs. (f) IR-PHI spectra of individual, select MNP particles from (a–e) labeled particles 1, 2, 3, and 4 (solid-colored lines) and an ATR–FTIR spectrum of a bulk 95 °C steeped nylon tea bag (dashed black line). The nylon amide I band with a peak at 1637 cm⁻¹ is highlighted in red. Spectra are offset for clarity.

shows a resulting IR-PHI image, a $20 \times 20~\mu\text{m}^2$ false color scan, where the peak signal (red) represents a higher normalized IR absorption intensity for the characteristic frequency selected (1720 cm⁻¹). The presence of numerous particles of varying sizes was observed. Figure 1c shows the resulting size distribution histogram from an analysis of approximately 200 particles (12 $20 \times 20~\mu\text{m}^2$ IR-PHI scanned areas). An average particle radius was $371 \pm 65~\text{nm}$. The size analysis does not include aggregated particles that are formed upon sample drying (Figure S4a). The theoretical size of the PMMA microspheres as reported by the manufacturer is $375~\text{nm} \pm 10\%$. The large size variation as measured by IR-PHI was attributed to error in the manufacturer's size estimation, with our SEM analysis revealing a size variation larger than 10% (Figure S4b).

Blind samples 1 and 2 had theoretical concentrations of 1.75 \times 10⁸ and 8.75 \times 10⁸ microspheres mL⁻¹, respectively, as determined from the manufacturer's reported values. IR-PHI analysis yields 1.18 \times 10⁸ and 5.48 \times 10⁸ microspheres mL⁻¹, corresponding to an approximate undercounting of 33 and 37%, respectively. Differences between actual and theoretical sizes can be attributed to errors in the manufacturer's concentrations and limitations with current image processing algorithms that do not fully account for aggregated particles (i.e., Figure S4a).

Analysis of Nylon Tea Bags Steeped at 95 °C. Figure 2 shows IR-PHI and SEM data for samples prepared from nylon

tea bags steeped in ultrapure water at 95 °C for 5 min. Nylon is an aliphatic polyamide (i.e., amide monomer links) identified by broad amide vibrational bands. An IR scan of various particles reveals these characteristic amide bands corresponding to amide I $(1620-1660 \text{ cm}^{-1}; \text{ peak } 1637 \text{ cm}^{-1})$, II (1530-1580 cm⁻¹; peak 1547 cm⁻¹), and III (1400-1480 cm⁻¹; peak 1434 cm⁻¹) bands (Figure 2f). The amide I band is dominated by C=O stretching, with minor contributions from out-of-phase CN stretching, in-plane NH bending, and CCN deformation. The amide II band is predominately out-of-phase in-plane NH bending with contributions from out-of-phase CN stretching, in-plane CO bending, CC stretching, and NC stretching. The amide III band is predominantly CN stretching and NH bending. The peak of the amide I band (1637 cm⁻¹) was chosen for IR-PHI imaging because of its predominance in the IR spectra.

Figure 2a—e depicts IR-PHI false-color images, where the peak signal (red) represents a higher normalized IR absorption intensity for the characteristic wavenumber (1637 cm⁻¹) corresponding to the spectra in Figure 2f. Figure 2a illustrates a 15 \times 15 μ m² scan containing four particles, and Figure 2b shows an associated 6 \times 6 μ m² magnification of the two lower intensity particles to highlight IR-PHI's high degree of spatial resolution. Particle 2 actually consists of three discrete particles, which was revealed with our deconvolution post-processing of the image (e.g., Figure S2). Figure 2c shows a larger 50 \times 50 μ m² image of the same sample illustrating the

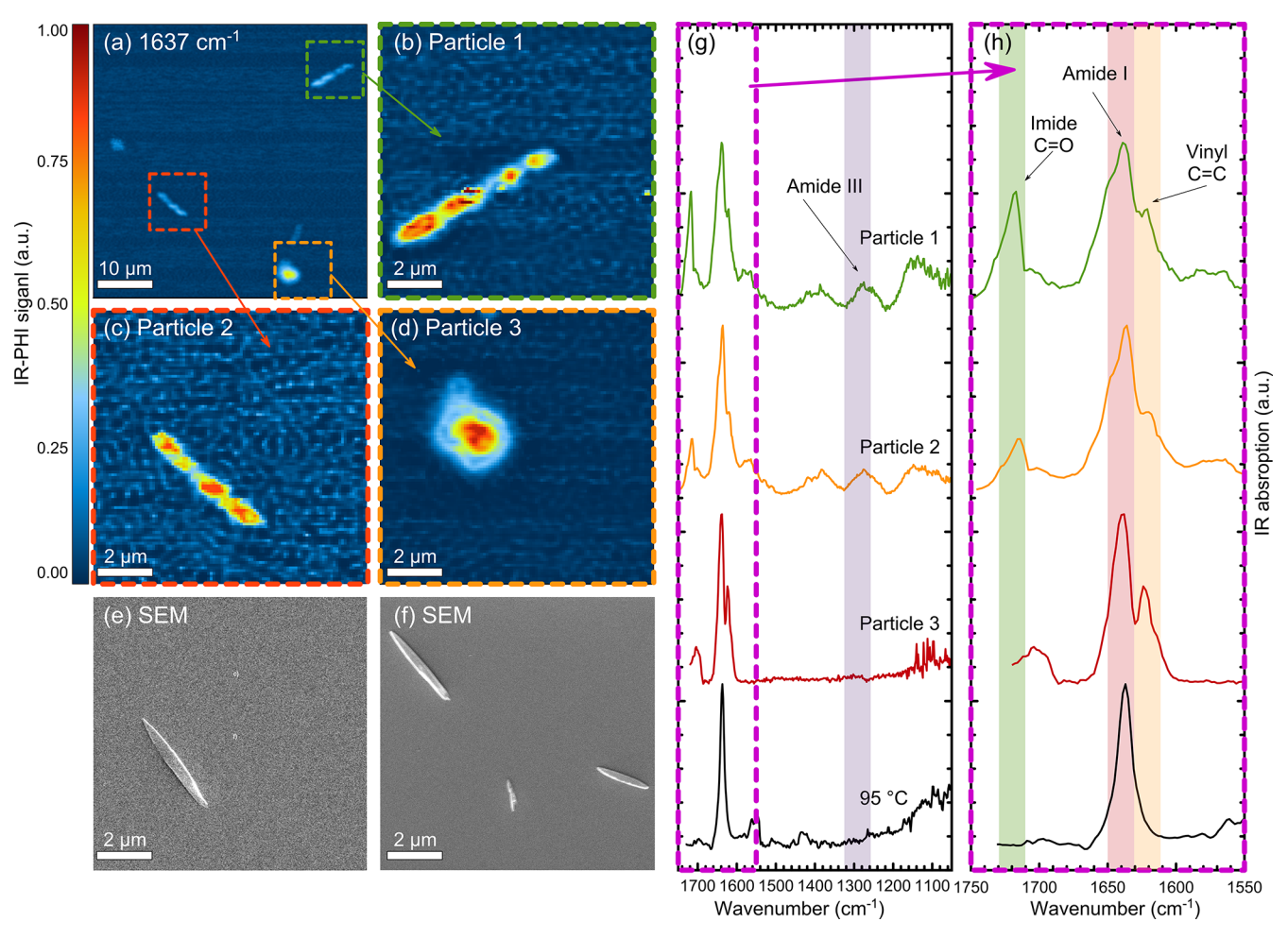


Figure 3. Analysis of MNPs from nylon tea bags steeped at 25 °C. All IR-PHI images were analyzed at 1637 cm⁻¹. (a) Low-magnification (50 × 50 μ m²) IR-PHI image highlighting three particles. (b-d) Deconvoluted, (10 × 10 μ m²) high-magnification IR-PHI images of select particles (1-3) from (a). (e,f) High magnification 10 × 10 μ m² SEM image of MNPs. (g) IR-PHI spectra of particles 1-3 (solid green, orange, and red lines, respectively) at 25 °C and particle 4 at 95 °C from Figure 2 for reference (solid black line). (h) Spectral zoom-in of the purple highlighted region in panel (g). Orange (1616–1624 cm⁻¹), red (1630–1650 cm⁻¹), and green (1715 cm⁻¹) highlighted regions indicate C=C stretch, amide I (i.e., C=O dominant), and C=O stretch vibrations, respectively. All IR-PHI spectra are offset for clarity.

ability to map intensities as a three-dimensional plot to easily highlight potential particles. Figure 2d,e shows a 15 \times 15 $\mu\mathrm{m}^2$ magnified image of two regions of interest containing particles of varying sizes. In all cases, the selected particles in Figure 2a–e (i.e., particles 1–4) have near identical IR features corresponding to nylon, with amide I, II, and III bands highlighted in Figure 2f. Bulk ATR–FTIR analysis on the tea bags (Figure 2f, bottom) shows similar characteristics as IR-PHI, but some of the sensitivity is lost due to the presence of unknown compounds contributing to the bulk spectra. Although an FTIR microscope possesses a better spatial resolution than conventional ATR–FTIR, the average response of an ensemble of MNPs is still reported due to its \sim 5 $\mu\mathrm{m}$ spatial resolution. This underlines the usefulness of IR-PHI to obtain the chemical composition of only particles of interest.

Figures 2a—e and S5 show that the effective radius of the nylon MNPs as determined by IR-PHI varied widely from approximately 303 to 1260 nm (a mean of 554 \pm 480 nm; N = 20 particles). IR-PHI size analysis is compared to SEM images shown in Figures 2g and S6. The effective radius calculated from the SEM analysis was approximately 60 to 1300 nm (N = 1558 particles), with a bimodal distribution around ~85 (83 \pm

36) and \sim 1050 nm (1063 \pm 497 nm). Sizing results from IR-PHI and SEM analyses are summarized by a histogram distribution in Figure S7. Of note in the SEM images was the prevalence of particles with radii smaller than 30 nm, which is below the current detection limit of IR-PHI and will result in undercounting by IR-PHI when compared to SEM.

Total MNP particle counts, as determined from the IR-PHI and SEM images (Figures 2a–g and S6), were approximately 4.5×10^8 and 7.5×10^{10} particles, respectively. The concentration resulting from SEM analysis of particles less than 3 μ m was approximately 10^2 times greater than that established via IR-PHI analysis. In a size range similar to that used by IR-PHI (~300 to 1300 nm), the concentration of particles as determined from SEM analysis was 6×10^9 particles (N = 115 particles), or just 1 order of magnitude difference. To reiterate though, SEM analysis does not have chemical specificity and counts every particle present in solution, whereas, IR-PHI only counts particles with characteristic vibrations at 1637 cm⁻¹. In comparison, Hernandez et al. used SEM to analyze particles sized from \sim 1 nm to 150 μ m that were released from a nylon tea bag steeped at 95 °C and counted approximately 1.5×10^{10} particles. ¹⁷ Thus, values from the two SEM analyses are within an order of magnitude.

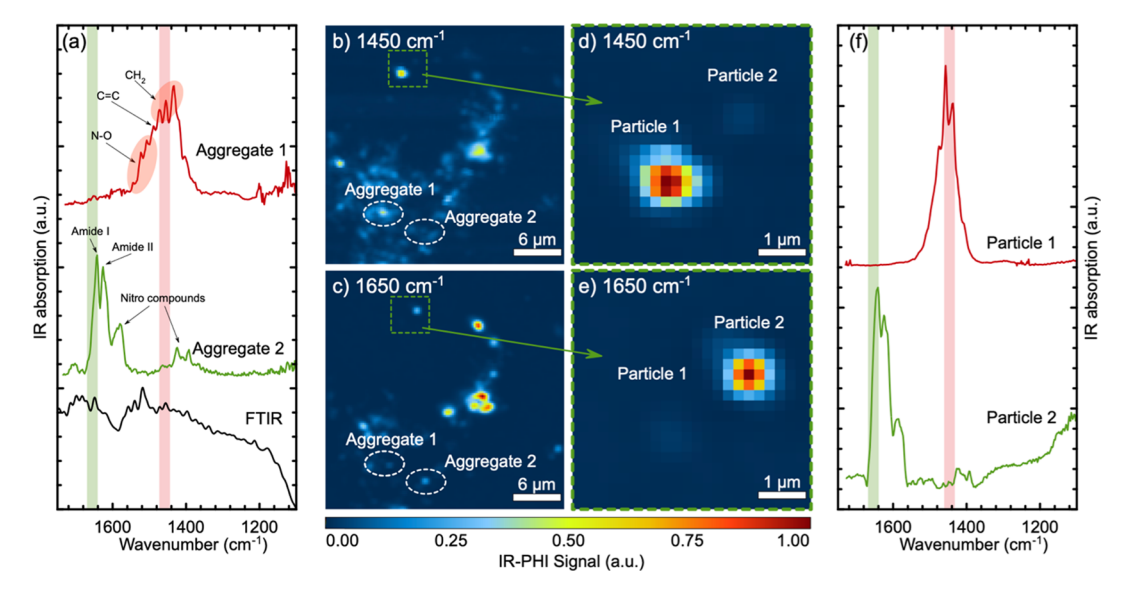


Figure 4. (a) FTIR spectrum of bulk road dust (solid black line) and IR-PHI spectra of individual road dust aggregates, labeled aggregates 1 and 2 (solid red and green lines, respectively). (b,c) $30 \times 30 \ \mu\text{m}^2$ IR-PHI images of road dust acquired at (b) 1450 and (c) 1650 cm⁻¹. (d,e) $5 \times 5 \ \mu\text{m}^2$ magnified images of highlighted regions of interest from (b,c). (f) Corresponding IR-PHI spectra of particles 1 and 2. For both (a,f), red (1450 $\pm 7 \ \text{cm}^{-1}$) and green (1650 $\pm 7 \ \text{cm}^{-1}$) vertical highlights indicate the frequencies used to acquire images (b,d and c,e), respectively. Spectra are offset for clarity.

The observed discrepancy may stem from measurements conducted using nylon tea bags from different manufacturers, variations in the sample preparation, or differences in the counting approach, which in our case, was based on the signal threshold set as two times the standard deviation of the background noise.

Chemical and Morphological Differences of Nylon Tea Bags Steeped at 25 °C. Nylon tea bags were steeped at room temperature (\sim 25 $^{\circ}$ C) to demonstrate IR-PHI's ability to detect morphological and chemical changes upon heating. IR-PHI analysis was conducted using the same IR peak at 1637 cm⁻¹ identified previously for nylon. Figures 3a-d and S8 show IR-PHI images of tea bag specimens steeped at 25 °C. The morphology of MNP particles was predominated by fiberlike shapes, which contrasted with the primarily quasi-spherical MNPs detected in samples steeped at 95 °C (Figure 2). Fiberlike morphologies were confirmed using SEM analysis (Figures 3e,f and S9). Observed MNPs have particle lengths from \sim 1 to 10 µm. Particle concentrations obtained from IR-PHI and SEM images were 8.3×10^5 and 1.7×10^7 particles mL⁻¹, respectively, confirming that MNPs are released from tea bags simply by soaking them in room-temperature water. Observed differences with IR-PHI again likely stem from IR-PHI's ~300 nm spatial resolution and SEM's lack of chemical specificity. The particle concentration at 25 °C was approximately fourfold lower than that at 95 °C, confirming thermal degradation and particle release from steeping nylon tea bags at increased temperatures.

Figure 3g and the accompanying spectral zoom-in for 1550 to 1750 cm⁻¹ (Figure 3h) show the associated IR spectra of particles 1–3 from IR-PHI images in Figure 3a–d. As a comparison, the IR spectrum of particle 4 from Figure 1 that was released at 95 °C is also shown. Compared to the bulk FTIR, the single-particle IR-PHI allowed for a more detailed analysis of MNP chemical changes (Figure S10). Samples steeped at 25 °C had similar amide I and II bands as those steeped at 95 °C with partial amide III resonances also present. MNPs from samples steeped at 25 °C, however, possessed

increased relative peak intensities and new features highlighted in Figure 3h. This includes an increased intensity and broadening of the amide III band between 1220 and 1320 $\rm cm^{-1}$ (purple shaded region), an additional shoulder in the amide I region at $\sim\!1620~\rm cm^{-1}$ (orange shaded region), and a new feature at $\sim\!1715~\rm cm^{-1}$ (green shaded region). These spectral alterations indicate thermally induced chemical changes to the MNPs that can be linked to observed morphological changes.

The features centered at 1620 and 1715 cm⁻¹ are not characteristic of pure nylon. 49 These regions are attributed to saturated C=O stretching in numerous other compound classes (e.g., aldehydes, ketones, esters, and carboxylic acids) and to C=C stretching. Prior literature on the degradation of nylon suggests that thermal treatment leads to products that possess IR transitions distinct from its pure state. 10,50 Both Do et al. 10 and Gocalves et al. 50 report that an oxidative attack on nylon's N-vicinal (alpha) carbons from thermal degradation results in species containing imide (C=O) and vinyl (C=C) functional groups. The former exhibits a resonance at ~1740 cm⁻¹, while the latter occurs at 1628 cm⁻¹. These match the features identified by IR-PHI at ~1715 and 1620 cm⁻¹ for MNPs released from nylon tea bags steeped at 25 °C (orange and green vertical highlights, Figures 3f and S10). Presumably, for the 25 °C sample, the thermal degradation byproducts identified by IR-PHI are an artifact of the manufacturing process of nylon fibers drawn using a heated process (melt temperature 220 to 260 °C).51

The amide III feature at 1220–1320 cm⁻¹ for the 25 °C sample disappears upon heating (Figures 3g and S10). Do et al. and Gocalves et al. point to the continued chemistry of the thermal degradation byproduct containing imide and vinyl groups that results in chain scission and leads to the production of a wide variety of small-molecule products. This explains loss of the 1220–1320 cm⁻¹ amide III band for the 95 °C sample as the *N*-vicinal methylene C–N bond is broken. It also explains the fiber-to-particulate morphological changes observed between 25 and 95 °C MNPs.

Using single-particle IR-PHI, we were therefore able to identify specific chemical alterations to the nylon MNPs that were not featured in the bulk FTIR analysis. IR-PHI analysis suggests that manufacturing thermal degradation byproducts are present in nylon tea bags. These products are eliminated during the steeping process at 95 °C. Further, IR-PHI was able to link chemical changes related to polymer chain scission with morphological changes that occurred upon heating the tea bag.

IR-PHI Analysis of Road Dust. Road dust contains MNPs resulting from tire degradation 41,52 that are composed of natural 33 and synthetic rubbers 54,55 and nylon. 56 Synthetic rubbers are used to enhance tire cushioning and elasticity, 42 while nylon is used in tire inner liners. Road dust additionally contains N-O-containing nitro compounds from fuel additives. 57

In the current study, bulk road dust was first characterized by acquiring its bulk FTIR spectrum (Figure 4a). This analysis showed a broad continuum of unresolved transitions between 1100 and 1750 cm⁻¹, which suggests a complex mixture of materials. Because rubber possesses a characteristic CH₂ bending mode at ~1450 cm⁻¹ (vertical red highlight),⁵³ this frequency was chosen for initial IR-PHI imaging analysis. Figure 4b shows a resulting 30 \times 30 μ m² IR-PHI image at 1450 cm⁻¹, where dense aggregates and single particles of road dust are seen. Two aggregate regions (aggregates 1 and 2) and two single particles (particle 1 and 2) were highlighted for further IR analysis. The corresponding spectra for aggregates 1 and 2 depicted in Figure 4a reveal chemical heterogeneity, exhibiting predominant transitions between 1400-1520 and 1560-1660 cm⁻¹. This, in turn, translates into image differences when IR-PHI imaging measurements were conducted at 1650 cm⁻¹; the peak frequency for aggregate 2 is shown in Figure 4c.

Spectral analysis suggests that aggregate 1 was primarily composed of synthetic rubber given dominant features at 1451 \pm 4 and 1493 \pm 4 cm^{-1.58} Nitro compounds with transitions between 1500 and 1550 cm⁻¹ were also present. Aggregate 2 possessed dominant amide I and II transitions characteristic of nylon. It also had transitions consistent with nitro-containing compounds such as nitromethane (1383 and 1573 cm⁻¹). Aggregate 2 also presumably contained nitrogen-containing biological compounds with a prominent spectral shoulder at 1570–1580 cm⁻¹ assigned to 2-aminooctanoic acid. These preliminary road dust spectral assignments are summarized in Table S1.

To identify more specific IR features and illustrate the ability of IR-PHI to spatially resolve chemical heterogeneity within complex matrices, single particles 1 and 2 highlighted in Figure 4a were further analyzed. Figure 4d,e shows $5 \times 5 \mu m^2$ IR-PHI images for 1450 and 1650 cm⁻¹ spectral features, respectively. At 1450 cm⁻¹, particle 1 is chemically distinct from particle 2, and the corresponding IR analysis in Figure 4f confirms a dominant band from ~1400 to 1520 cm⁻¹, which is similar to features present in aggregate 1. Similarly, at 1650 cm⁻¹, particle 2 is distinct from particle 1 and has IR features (Figure 4f) similar to aggregate 2. Thus, particle 1 and particle 2 are presumably composed of rubber and nylon, respectively.

Herein, we have demonstrated IR-PHI's ability to quantify MNPs, monitor chemical changes that occur during degradation, and characterize the chemical identity of single and aggregate MNPs present in complex samples (i.e., road dust). Due to the chemical specificity of IR-PHI, no special sample preparation was required. The technique overcomes many

current limitations that restrict MNP characterization, namely, the ability to simultaneously quantify particle abundance and morphology, both with chemical specificity. This points to the potential future use of IR-PHI as a key tool for analyzing MNPs in real-world, spectroscopically congested environments.

ASSOCIATED CONTENT

Supporting Information

The Supporting Information is available free of charge at https://pubs.acs.org/doi/10.1021/acs.est.1c05181.

Details of IR-PHI operation and particle counting and sizing, mathematical details of the Richardson–Lucy image deconvolution, detailed comparison of the original and deconvoluted images taken by IR-PHI, SEM images of the PMMA microbeads, additional IR-PHI spectra and images of the individual MNP particles from nylon tea bags steeped at 25 and 95 °C, size distribution histogram of the SEM and IR-PHI image analyses, and IR band assignments for road dust MNPs (PDF)

AUTHOR INFORMATION

Corresponding Authors

Kyle Doudrick — Department of Civil and Environmental Engineering and Earth Sciences, University of Notre Dame, Notre Dame, Indiana 46556, United States; ⊚ orcid.org/0000-0003-1912-9819; Phone: 5746310305; Email: kdoudrick@nd.edu

Masaru Kuno — Department of Chemistry and Biochemistry, University of Notre Dame, Notre Dame, Indiana 46556, United States; Department of Physics, University of Notre Dame, Notre Dame, Indiana 46556, United States; orcid.org/0000-0003-4210-8514; Email: mkuno@nd.edu

Authors

Kirill Kniazev – Department of Chemistry and Biochemistry, University of Notre Dame, Notre Dame, Indiana 46556, United States

Ilia M. Pavlovetc – Department of Chemistry and Biochemistry, University of Notre Dame, Notre Dame, Indiana 46556, United States

Shuang Zhang — Department of Electrical Engineering, University of Notre Dame, Notre Dame, Indiana 46556, United States

Junyeol Kim — Department of Civil and Environmental Engineering and Earth Sciences, University of Notre Dame, Notre Dame, Indiana 46556, United States; Department of Civil and Environmental Engineering, Wayne State University, Detroit, Michigan 48202, United States

Robert L. Stevenson — Department of Electrical Engineering, University of Notre Dame, Notre Dame, Indiana 46556, United States

Complete contact information is available at: https://pubs.acs.org/10.1021/acs.est.1c05181

Notes

The authors declare no competing financial interest.

G

ACKNOWLEDGMENTS

M.K. thanks the National Science Foundation (CHE-1563528 and CHE-1954724) for financial support of this study. K.D. thanks the National Science Foundation (CBET-1705770) for financial support of this study.

REFERENCES

- (1) Hale, R. C.; Seeley, M. E.; La Guardia, M. J.; Mai, L.; Zeng, E. Y. A Global Perspective on Microplastics. *J. Geophys. Res.: Oceans* **2020**, 125, No. e2018JC014719.
- (2) Obbard, R. W.; Sadri, S.; Wong, Y. Q.; Khitun, A. A.; Baker, I.; Thompson, R. C. Global Warming Releases Microplastic Legacy Frozen in Arctic Sea Ice. *Earth's Future* **2014**, *2*, 315–320.
- (3) Triebskorn, R.; Braunbeck, T.; Grummt, T.; Hanslik, L.; Huppertsberg, S.; Jekel, M.; Knepper, T. P.; Krais, S.; Müller, Y. K.; Pittroff, M.; Ruhl, A. S.; Schmieg, H.; Schür, C.; Strobel, C.; Wagner, M.; Zumbülte, N.; Köhler, H. R. Relevance of Nano- and Microplastics for Freshwater Ecosystems: A Critical Review. *Trends Anal. Chem.* **2019**, *110*, 375–392.
- (4) Van Cauwenberghe, L.; Janssen, C. R. Microplastics in Bivalves Cultured for Human Consumption. *Environ. Pollut.* **2014**, 193, 65–70.
- (5) Scircle, A.; Cizdziel, J. V. Detecting and Quantifying Microplastics in Bottled Water Using Fluorescence Microscopy: A New Experiment for Instrumental Analysis and Environmental Chemistry Courses. *J. Chem. Educ.* **2020**, *97*, 234–238.
- (6) Ragusa, A.; Svelato, A.; Santacroce, C.; Catalano, P.; Notarstefano, V.; Carnevali, O.; Papa, F.; Rongioletti, M. C. A.; Baiocco, F.; Draghi, S.; D'Amore, E.; Rinaldo, D.; Matt a, M.; Giorgini, E. Plasticenta: First Evidence of Microplastics in Human Placenta. *Environ. Int.* **2021**, *146*, 106274.
- (7) Anbumani, S.; Kakkar, P. Ecotoxicological effects of microplastics on biota: a review. *Environ. Sci. Pollut. Res.* **2018**, *25*, 14373–14396.
- (8) Wang, W.; Ge, J.; Yu, X. Bioavailability and Toxicity of Microplastics to Fish Species: A Review. *Ecotoxicol. Environ. Saf.* **2020**, 189, 109913.
- (9) Wang, W.; Gao, H.; Jin, S.; Li, R.; Na, G. The Ecotoxicological Effects of Microplastics on Aquatic Food Web, from Primary Producer to Human: A Review. *Ecotoxicol. Environ. Saf.* **2019**, *173*, 110–117.
- (10) Do, C. H.; Pearce, E. M.; Bulkin, B. J.; Reimschuessel, H. K. FT-IR spectroscopic study on the thermal and thermal oxidative degradation of nylons. *J. Polym. Sci., Part A: Polym. Chem.* **1987**, 25, 2409–2424.
- (11) De Gracia Lux, C.; McFearin, C. L.; Joshi-Barr, S.; Sankaranarayanan, J.; Fomina, N.; Almutairi, A. Single UV or near IR Triggering Event Leads to Polymer Degradation into Small Molecules. ACS Macro Lett. 2012, 1, 922–926.
- (12) Dos Santos, K.A.M.; Suarez, P.A.Z.; Rubim, J.C. Photo-Degradation of Synthetic and Natural Polyisoprenes at Specific UV Radiations. *Polym. Degrad. Stab.* **2005**, *90*, 34–43.
- (13) Tiede, K.; Boxall, A. B. A.; Tear, S. P.; Lewis, J.; David, H.; Hassellöv, M. Detection and Characterization of Engineered Nanoparticles in Food and the Environment. Food Addit. Contam., Part A: Chem., Anal., Control, Exposure Risk Assess. 2008, 25, 795–821.
- (14) Shim, W. J.; Hong, S. H.; Eo, S. E. Identification Methods in Microplastic Analysis: A Review. *Anal. Methods* **2017**, *9*, 1384–1391.
- (15) Chen, G.; Fu, Z.; Yang, H.; Wang, J. An Overview of Analytical Methods for Detecting Microplastics in the Atmosphere. *Trends Anal. Chem.* **2020**, *130*, 115981.
- (16) Erni-Cassola, G.; Gibson, M. I.; Thompson, R. C.; Christie-Oleza, J. A. Lost, but Found with Nile Red: A Novel Method for Detecting and Quantifying Small Microplastics (1 mm to 20 μ m) in Environmental Samples. *Environ. Sci. Technol.* **2017**, *51*, 13641–13648.
- (17) Hernandez, L. M.; Xu, E. G.; Larsson, H. C. E.; Tahara, R.; Maisuria, V. B.; Tufenkji, N. Plastic Teabags Release Billions of

- Microparticles and Nanoparticles into Tea. Environ. Sci. Technol. 2019, 53, 12300-12310.
- (18) Dümichen, E.; Barthel, A. K.; Braun, U.; Bannick, C. G.; Brand, K.; Jekel, M.; Senz, R. Analysis of Polyethylene Microplastics in Environmental Samples, Using a Thermal Decomposition Method. *Water Res.* **2015**, *85*, 451–457.
- (19) Vianello, A.; Boldrin, A.; Guerriero, P.; Moschino, V.; Rella, R.; Sturaro, A.; Da Ros, L. Microplastic Particles in Sediments of Lagoon of Venice, Italy: First Observations on Occurrence, Spatial Patterns and Identification. *Estuarine, Coastal Shelf Sci.* **2013**, *130*, 54–61.
- (20) Käppler, A.; Fischer, D.; Oberbeckmann, S.; et al.et al. Analysis of environmental microplastics by vibrational microspectroscopy: FTIR, Raman or both? *Anal. Bioanal. Chem.* **2016**, 408, 8377–8391.
- (21) Schymanski, D.; Goldbeck, C.; Humpf, H. U.; Fürst, P. Analysis of Microplastics in Water by Micro-Raman Spectroscopy: Release of Plastic Particles from Different Packaging into Mineral Water. *Water Res.* 2018, 129, 154–162.
- (22) Lenz, R.; Enders, K.; Stedmon, C. A.; MacKenzie, D. M. A.; Nielsen, T. G. A. A critical assessment of visual identification of marine microplastic using Raman spectroscopy for analysis improvement. *Mar. Pollut. Bull.* **2015**, *100*, 82–91.
- (23) Tagg, A. S.; Sapp, M.; Harrison, J. P.; Ojeda, J. J. Identification and Quantification of Microplastics in Wastewater Using Focal Plane Array-Based Reflectance Micro-FT-IR Imaging. *Anal. Chem.* **2015**, *87*, 6032–6040.
- (24) Tagg, A. S.; Sapp, M.; Harrison, J. P.; Sinclair, C. J.; Bradley, E.; Ju-Nam, Y.; Ojeda, J. J. Microplastic Monitoring at Different Stages in a Wastewater Treatment Plant Using Reflectance Micro-FTIR Imaging. Front. Environ. Sci. 2020, 8, 145.
- (25) Mintenig, S.M.; Int-Veen, I.; Löder, M.G.J.; Primpke, S.; Gerdts, G. Identification of microplastic in effluents of waste water treatment plants using focal plane array-based micro-Fourier-transform infrared imaging. *Water Res.* **2017**, *108*, 365–372.
- (26) Cho, H.; Baker, B. R.; Wachsmann-Hogiu, S.; Pagba, C. V.; Laurence, T. A.; Lane, S. M.; Lee, L. P.; Tok, J. B. H. Aptamer-based SERRS sensor for thrombin detection. *Nano Lett.* **2008**, *8*, 4386.
- (27) Pavlovetc, I. M.; Aleshire, K.; Hartland, G. V.; Kuno, M. Approaches to Mid-Infrared, Super-Resolution Imaging and Spectroscopy. *Phys. Chem. Chem. Phys.* **2020**, 22, 4313–4325.
- (28) Pavlovetc, I. M.; Podshivaylov, E. A.; Chatterjee, R.; Hartland, G. V.; Frantsuzov, P. A.; Kuno, M. Infrared Photothermal Heterodyne Imaging: Contrast Mechanism and Detection Limits. *J. Appl. Phys.* **2020**, *127*, 165101.
- (29) Bai, Y.; Yin, J.; Cheng, J. X. Bond-Selective Imaging by Optically Sensing the Mid-Infrared Photothermal Effect. *Sci. Adv.* **2021**, *7*, 1559–1573.
- (30) Li, Z.; Aleshire, K.; Kuno, M.; Hartland, G. V. Super-Resolution Far-Field Infrared Imaging by Photothermal Heterodyne Imaging. *J. Phys. Chem. B* **2017**, *121*, 8838–8846.
- (31) Li, X.; Zhang, D.; Bai, Y.; Wang, W.; Liang, J.; Cheng, J. X. Fingerprinting a Living Cell by Raman Integrated Mid-Infrared Photothermal Microscopy. *Anal. Chem.* **2019**, *91*, 10750–10756.
- (32) Aleshire, K.; Pavlovetc, I. M.; Collette, R.; Kong, X. T.; Rack, P. D.; Zhang, S.; Masiello, D. J.; Camden, J. P.; Hartland, G. V.; Kuno, M. Far-Field Midinfrared Superresolution Imaging and Spectroscopy of Single High Aspect Ratio Gold Nanowires. *Proc. Natl. Acad. Sci. U.S.A.* **2020**, *117*, 2288–2293.
- (33) Chatterjee, R.; Pavlovetc, I. M.; Aleshire, K.; Hartland, G. V.; Kuno, M. Subdiffraction Infrared Imaging of Mixed Cation Perovskites: Probing Local Cation Heterogeneities. *ACS Energy Lett.* **2018**, 3, 469–475.
- (34) Pavlovetc, I. M.; Brennan, M. C.; Draguta, S.; Ruth, A.; Moot, T.; Christians, J. A.; Aleshire, K.; Harvey, S. P.; Toso, S.; Nanayakkara, S. U.; Messinger, J.; Luther, J. M.; Kuno, M. Suppressing Cation Migration in Triple-Cation Lead Halide Perovskites. ACS Energy Lett. 2020, 5, 2802—2810.
- (35) Zhang, D.; Li, C.; Zhang, C.; Slipchenko, M. N.; Eakins, G.; Cheng, J. X. Depth-Resolved Mid-Infrared Photothermal Imaging of

- Living Cells and Organisms with Submicrometer Spatial Resolution. *Sci. Adv.* **2016**, *2*, No. e1600521.
- (36) Zhang, Y.; Yurdakul, C.; Devaux, A. J.; Wang, L.; Xu, X. G.; Connor, J. H.; Ünlü, M. S.; Cheng, J.-X. Vibrational Spectroscopic Detection of a Single Virus by Mid-Infrared Photothermal Microscopy. *Anal. Chem.* **2021**, *93*, 4100–4107.
- (37) Lim, J. M.; Park, C.; Park, J. S.; Kim, C.; Chon, B.; Cho, M. Cytoplasmic Protein Imaging with Mid-Infrared Photothermal Microscopy: Cellular Dynamics of Live Neurons and Oligodendrocytes. J. Phys. Chem. Lett. 2019, 10, 2857–2861.
- (38) Bai, Y.; Zhang, D.; Li, C.; Liu, C.; Cheng, J.-X. Bond-Selective Imaging of Cells by Mid-Infrared Photothermal Microscopy in High Wavenumber Region. *J. Phys. Chem. B* **2017**, *121*, 10249–10255.
- (39) Sieber, R.; Kawecki, D.; Nowack, B. Dynamic Probabilistic Material Flow Analysis of Rubber Release from Tires into the Environment. *Environ. Pollut.* **2020**, 258, 113573.
- (40) Hartmann, N. B.; Hüffer, T.; Thompson, R. C.; Hassellöv, M.; Verschoor, A.; Daugaard, A. E.; Rist, S.; Karlsson, T.; Brennholt, N.; Cole, M.; Herrling, M. P.; Hess, M. C.; Ivleva, N. P.; Lusher, A. L.; Wagner, M. Are We Speaking the Same Language? Recommendations for a Definition and Categorization Framework for Plastic Debris. *Environ. Sci. Technol.* **2019**, 53, 1039–1047.
- (41) Kole, P. J.; Löhr, A. J.; Van Belleghem, F. G. A. J.; Ragas, A. M. J. Wear and Tear of Tyres: A Stealthy Source of Microplastics in the Environment. *Int. J. Environ. Res. Public Health* **2017**, *14*, 1265.
- (42) Mengistu, D.; Nilsen, V.; Heistad, A.; Kvaal, K. Detection and Quantification of Tire Particles in Sediments Using a Combination of Simultaneous Thermal Analysis, Fourier Transform Infra-Red, and Parallel Factor Analysis. *Int. J. Environ. Res. Public Health* **2019**, *16*, 3444.
- (43) Article 311 Service Portal. https://311.southbendin.gov/knowledgecenter/article/?id=KA-04598 (accessed Jun 29, 2021).
- (44) Richardson, W. H. Bayesian-Based Iterative Method of Image Restoration. J. Opt. Soc. Am. 1972, 62, 55-59.
- (45) Lucy, L. B. An Iterative Technique for the Rectification of Observed Distributions. *Astron. J.* **1974**, *79*, 745.
- (46) van der Walt, S.; Schönberger, J. L.; Nunez-Iglesias, J.; Boulogne, F.; Warner, J. D.; Yager, N.; Gouillart, E.; Yu, T. scikitimage: image processing in Python. *PeerJ* **2014**, *2*, No. e453.
- (47) Jung, M. R.; Horgen, F. D.; Orski, S. V.; Rodriguez, C. V.; Beers, K. L.; Balazs, G. H.; Jones, T. T.; Work, T. M.; Brignac, K. C.; Royer, S.-J.; Hyrenbach, K. D.; Jensen, B. A.; Lynch, J. M. Validation of ATR FT-IR to Identify Polymers of Plastic Marine Debris, Including Those Ingested by Marine Organisms. *Mar. Pollut. Bull.* 2018, 127, 704–716.
- (48) Nasr-Esfahani, M.; Mehrabanian, M. HA/nylon 6,6 porous scaffolds fabricated by salt-leaching/solvent casting technique: effect of nano-sized filler content on scaffold properties. *Int. J. Nanomed.* **2011**, *6*, 1651–1659.
- (49) Vasanthan, N. Crystallinity Determination of Nylon 66 by Density Measurement and Fourier Transform Infrared (FTIR) Spectroscopy. *J. Chem. Educ.* **2012**, *89*, 387–390.
- (50) Gonçalves, E. S.; Poulsen, L.; Ogilby, P. R. Mechanism of the Temperature-Dependent Degradation of Polyamide 66 Films Exposed to Water. *Polym. Degrad. Stab.* **2007**, *92*, 1977–1985.
- (51) Campbell, I. M. Introduction to Synthetic Polymers, 2nd ed.; Oxford University Press, 2000.
- (52) Panko, J. M.; Chu, J.; Kreider, M. L.; Unice, K. M. Measurement of Airborne Concentrations of Tire and Road Wear Particles in Urban and Rural Areas of France, Japan, and the United States. *Atmos. Environ.* **2013**, *72*, 192–199.
- (53) Gorassini, A.; Adami, G.; Calvini, P.; Giacomello, A. ATR-FTIR Characterization of Old Pressure Sensitive Adhesive Tapes in Historic Papers. *J. Cult. Herit.* **2016**, *21*, 775–785.
- (54) Bonilla-Cruz, J.; Hernández-Mireles, B.; Mendoza-Carrizales, R.; Ramírez-Leal, L. A.; Torres-Lubián, R.; Valle, L. F. R.; Paul, D. R.; Saldívar-Guerra, E. Chemical Modification of Butyl Rubber with Maleic Anhydride via Nitroxide Chemistry and Its Application in Polymer Blends. *Polymers* **2017**, *9*, 63.

I

- (55) Pticek, A.; Hrnjak-Murgic, Z.; Jelencic, J.; Mlinac-Misak, M. Morphology and thermal behaviour of SAN/EPDM blends. *eXPRESS Polym. Lett.* **2007**, *1*, 370.
- (56) Dipak, G. Radial tires containing polyamide monofilament. U.S. Patent 4,850,412 A, 1989. https://patentimages.storage.googleapis.com/8c/c5/42/818fa35604718a/US4850412.pdf.
- (57) Li, B.; Ma, L.-X.; Sun, S.-J.; Thapa, S.; Lu, L.; Wang, K.; Qi, H. Polycyclic Aromatic Hydrocarbons and Their Nitro-Derivatives in Urban Road Dust across China: Spatial Variation, Source Apportionment, and Health Risk. *Sci. Total Environ.* **2020**, *747*, 141194.
- (58) https://www.sigmaaldrich.com/US/en/technical-documents/technical-article/analytical-chemistry/photometry-and-reflectometry/ir-spectrum-table (retrieved Jun 29, 2021).
- (59) NIST Standard Reference Simulation Website, NIST Standard Reference Database Number 173; Shen, V. K., Siderius, D. W., Krekelberg, W. P., Hatch, H. W., Eds.; National Institute of Standards and Technology: Gaithersburg MD, 20899. (retrieved Jun 29, 2021).
- (60) National Center for Biotechnology Information (2021). PubChem Compound Summary for CID 69522, 2-Aminooctanoic acid. https://pubchem.ncbi.nlm.nih.gov/compound/2-Aminooctanoic-acid (retrieved Nov 1, 2021).